Strojniški vestnik - Journal of Mechanical Engineering 64(2018)6, 373-382
DOI:10.5545/sv-jme.2017.5120
Original Scientific Paper
Received for review: 2017-11-30
Received revised form: 2018-03-18
Accepted for publication: 2018-04-16

Fatigue Design of Ferritic-Pearlitic Nodular Cast Iron Components with Surface Discontinuities

Márton Gróza* – Károly Váradi
Budapest University of Technology and Economics, Department of Machine and Product Design, Hungary

Surface and subsurface discontinuities are one of the most important factors affecting the fatigue life of structural cast components. Their location, shape and size vary from component to component, most of them are completely harmless, but one critical defect can lead to in-service failure. Allowable surface discontinuity size finite element (FE) results can be a practical engineering tool for casting design, process planning, and the quality inspection process. Different methods based on the continuum and fracture mechanics applicable on the multiaxial high-cycle fatigue (HCF) and fatigue limit prediction for components with surface discontinuities are compared with experimental results on ISO1083/JS/500-7 nodular cast iron (NCI). Results also confirm, that the fatigue properties of the analysed material in standards truly represent low-end material strength. A design methodology is presented based on the Defect Stress Gradient approach for the display of an allowable surface discontinuity size FE-result for complex components under proportional loading conditions in HCF.
Keywords: high-cycle fatigue, finite element analysis, fracture mechanics, surface defects, multiaxial fatigue

Highlights
- *Fatigue test results for the ISO1083/JS/500-7 NCI material grade with and without surface discontinuities are compared and analysed.*
- *Different methods are applied to describe the reduction of fatigue strength with the equivalent surface discontinuity size.*
- *Allowable surface discontinuity size FE-results are plotted based on the DSG approach with the consideration of the mean-stress dependent scatter in the fatigue strength.*
- *The proposed method to obtain allowable surface discontinuity size results is directly applicable in industrial applications.*

0 INTRODUCTION

The numerous advantageous characteristics of nodular cast iron (NCI) components, such as their steel-like mechanical properties and economical manufacturability, are linked with a higher level of scatter in material behaviour compared to steels. Engineering materials are classified based on their minimum monotonic tensile properties; therefore, a given standardized NCI grade can contain materials with 100 MPa difference in tensile and fatigue strength. Recommended values for the fatigue strength in standards and design guidelines do not always correspond to the lower-end strength material with the prescribed minimum monotonic properties.

Apart from the large-scale scatter originating from differences in the microstructure and wall-thickness, internal and surface discontinuities also heavily influence the fatigue life of structural cast components. Surface and subsurface discontinuities have the most detrimental effect on the fatigue strength from these factors; their position, size, and morphology vary from component to component. A critical defect can lead to in-service failure, but most of the discontinuities do not affect the expected service life. A fatigue assessment-based quality inspection methodology is, therefore, necessary to balance in-service safety and the economical production of cast components. Allowable surface discontinuity size finite element (FE) result fields are a practical engineering tool during casting design, process planning, and the quality inspection process. The current study employs different methods to obtain the allowable surface discontinuity size as an FE-result field.

Improving the accuracy of the fatigue assessment calculations through the consideration of the non-idealistic properties of components is currently a heavily researched area. Nadot et al. **[1]** investigated the effect of casting defects of the fatigue limit of NCI material. From the standpoint of the defect-induced fatigue process, each specimen is considered individual during testing. For the assessment of individual fracture events, the "step-by-step" method proposed by Bellows et al. **[2]** has proven to be essential. Cheng et al. **[3]** the high frequency cut-off of machined surface topography is defined, which is related to a material parameter a0. Besides, the proposed analytical expressions are applied to predict the stress concentration factors (SCFs derived analytical formulas for the modelling of the surface topography in the fatigue assessment process based on the theory of critical distance. Rotella et al. **[4]** plotted a defect size map based on FE-calculations for cast A357-T6 under multiaxial loading using the defect stress gradient (DSG) criterion.

*Corr. Author's Address: BME, Department of Machine and Product Design, Műegyetem rkp. 3, Budapest 1111, Hungary groza.marton@gt3.bme.hu

The comparison of experimental and simulation results has shown that the DSG criterion provides a good estimation of the crack initiation sites. Vincent et al. [5] have shown that the defect size that impacts the fatigue limit is largely dependent on the grain size of the material. Schönbauer et al. [6] investigated small artificial surface defects on the torsional and tensile fatigue behaviour of precipitation-hardened chromium-nickel-copper stainless steel. They concluded, that fatigue behaviour is governed by the maximum principal stress even under torsion and emphasized the importance of the crack initiation phase for defects with $\rho \geq 50$ μm notch root radius. Mukherjee et al. [7] analysed the relationship between fatigue and microstructural properties in NCI material with cooling rate calculations, microstructural characterization by 2D SEM and 3D X-ray tomography and fatigue testing on sand and metal moulded samples.

Casting defects can be considered to be notches with complex morphology; most of the advancements in the area of notched fatigue research are, therefore, applicable with some modifications. The effect of notches on the crack initiation life can be approached from the standpoint of fracture mechanics with the analysis of short-crack propagation. Ostash et al. [8] applied a fracture mechanics approach for macrocrack initiation life computation on notched mild-steel and aluminium specimens with promising results. A conventional stress-strain based approach was applied in the work of Gates and Fatemi [9] for multiaxial notched fatigue analysis with the utilization of the theory of critical distances and the Fatemi-Socie critical plane damage parameter. New approaches are currently being developed for a unified description of the total fatigue life; Liu et al. [10] proposed a method based on the theory of damage mechanics to describe damage evolution in a notched specimen.

The current study compares different approaches to simulate the Kitagawa diagram (fatigue strength vs surface discontinuity size) for ISO1083/JS/500-7 NCI material. These methods are used to plot equivalent allowable surface discontinuity size FE-results. Experimental and literature fatigue data are compared to quantify the scatter in the defect-free fatigue properties. Design values of the surface discontinuity size-dependent fatigue strength are derived to ensure safety during the quality inspection process.

1 EXPERIMENTAL RESULTS FOR NCI MATERIAL

As part of a large-scale research program with the aim of improving the fatigue design of NCI components, load-controlled fatigue tests have been conducted on specimens with different microstructures and surface properties. The material chosen for this analysis is a ferritic-pearlitic NCI, designated as ISO1083/JS/500-7 according to the international standard ISO 1083 [11].

1.1 Results with Artificial Surface Defects and Casting Skin

One hundred (100) fatigue test specimens with a rectangular cross-section were created with a complex artificial surface defect introduced by means of a special casting core. Fig. 1 shows the specimen geometry and computed tomography (CT) image from the longitudinal cross-section. The equivalent size of the artificial complex defect is 2110 μm according to the $\sqrt{area}$ parameter from Murakami [12]. A detailed view of the surface defect in the specimens can be seen in Fig. 2. The chemical composition shown in Table 1 is consistent with the expectations to achieve a casting material for the ISO1083/JS/500-7 grade. In Table 1, Sc refers to the degree of saturation, and has been calculated as $Sc = \%C/(4.23 - 0.3 \cdot (\%Si + \%P))$. An evaluation of the obtained microstructural features in accordance to ISO 945-1 [13] is summarized in Table 2. The metallographic inspections were conducted on a cross-section of the clamping area from a tensile specimen. B8×40 (DIN 50125 [14]) tensile specimens have been machined to standard ISO 1083 Y1-shaped test samples with 265 mm length. The tensile tests were carried out at room temperature according to EN ISO 6892-1 [15]. The average values of 12 tensile tests are a proof strength of $R_{p0.2} = 348 \pm 21$ MPa, an ultimate tensile strength of and an elongation at fracture of $R_m = 583 \pm 43$ MPa and an elongation at fracture of $A = 14\ \% \pm 2\ \%$.

Table 1. *Average chemical composition of the test specimens (average of five measurements)*

%C	%Si	%Mn	%P	%S	%Cr	%Cu	%Mg	Sc
3.62	2.33	0.19	0.013	0.005	-	0.36	0.04	1.03

Table 2. *Average metallographic properties of the test specimens (average of five measurements)*

Graphite [%]	Nodules [1/mm²]	Nodularity [%]	Form III [%]	Form IV [%]	Form V [%]	Form VI [%]	Pearlite cont. [%]	Size
10.7±0.14	657±207	88.8±1	0.84±0.15	0.24±0.1	28±2.6	70.92±2.6	46.6±3.8	6

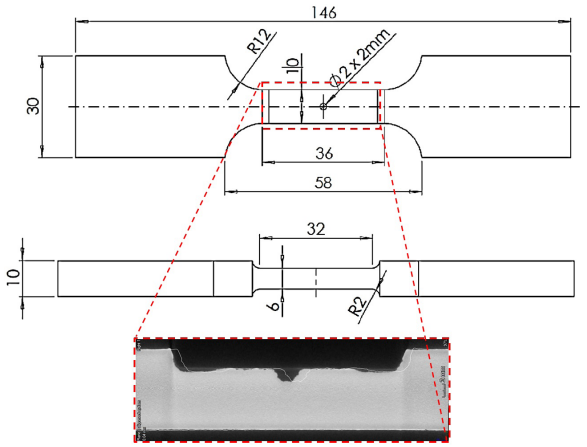

Fig. 1. *Fatigue test specimen with casting skin and complex artificial surface defect, CT image of the cross-section of the gauge length*

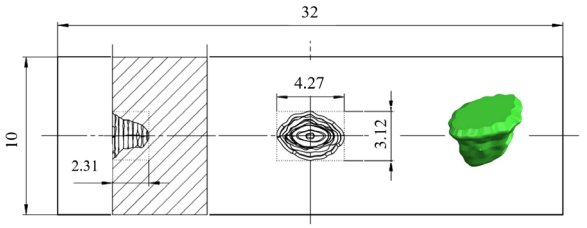

Fig. 2. *Geometry of the testing section of the fatigue test specimen with casting skin and complex artificial surface defect*

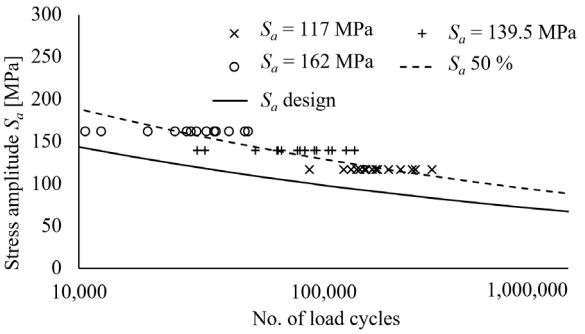

Fig. 3. *Design and 50 % failure probability S-N curves for defective ISO1083/JS/500-7 with the test results for $R_{0.1}$ pulsating tensile load*

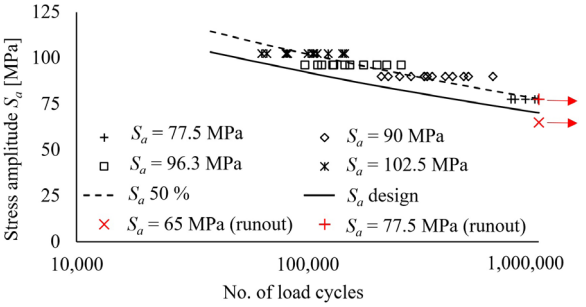

Fig. 4. *Design and 50 % failure probability S-N curves for defective ISO1083/JS/500-7 with the test results for $R_{0.5}$ pulsating tensile load*

Fatigue tests were carried out on a RUMUL MAGNODYN fatigue machine at room temperature at $R_{0.1}$ and $R_{0.5}$ pulsating tension loads with fixed amplitude with a testing frequency of 40 Hz. Cracks initiated exclusively from the large artificial defect.

Fig. 3 and 4 show the fitted and the design (97.5 % failure probability and 95 % significance level considering the lognormal distribution of fatigue life) S-N curves with the experimental data for $R_{0.1}$ and $R_{0.5}$ pulsating tension load.

1.2 Results for Low and High-Strength Material

Fatigue tests were conducted on low- and high-strength ISO1083/JS/500-7 material, to estimate the possible scatter in the high-cycle fatigue properties of smooth specimens. The specimens have been machined from NCI components from the production line, the distinction "low" and "high" strength refers to different batches of the same component. The tensile properties of the studied materials were determined on B8×40 (DIN 50125 [14]) tensile specimens according to the standard EN ISO 6892-1 [15] and are summarized in Table 3.

The geometries of the fatigue test specimens are displayed in Fig. 5. The fatigue tests were carried out on an INSTRON 8874 servo-hydraulic fatigue machine with a fixed-load ratio of R0.05 and a fixed-load maximum with a testing frequency of 30 Hz. In the case of the low-strength material, fatigue testing was carried out at three different stress levels to obtain the full S-N curve.

In the case of the high-strength cast iron, the step-by-step method [2] was applied with 20 MPa steps in the stress maximum to determine the fatigue strength at 10^6 cycles.

Fracture surfaces were analysed, and the initiation sites were located in the near-surface region without the influence of notable subsurface or internal defects. Results are summarized in Table 4.

It is interesting to note that the previous loading steps below the fatigue limit do not have a noticeable impact in the fatigue strength; therefore, the application of the step-by-step approach in the fatigue testing process is justified. Fig. 6 shows the obtained test results with the fitted S-N curve and the S-N curve based on the FKM guideline [16].

Table 3. *Summary of tensile monotonic and fatigue strength at cycles for the ISO1083/JS/500-7 cast iron material at different R-ratios*

Designation	$R_{p0.2}$ [MPa]	R_m [MPa]	A [%]	σ_{R-1} [MPa]	σ_{R0} [MPa]	$\sigma_{R0.05}$ [MPa]	$\sigma_{R0.1}$ [MPa]	$\sigma_{R0.36}$ [MPa]	$\sigma_{R0.5}$ [MPa]
FKM [16]	320	500	7	170	135	-	-	-	-
low-strength	328	491	15	(194)	-	135	-	-	-
high-strength	378	649	9.7	(277)	-	188	-	-	-
Yamabe and Kobayashi [17]	363	555	8	275	-	-	-	-	-
Rabb [18]	338	625	-	260	-	-	160	120	-
artificial defect	348	583	14	(119)	-	-	88	-	78

Table 4. *Fatigue test results for the high-strength ISO1083/JS/500-7 material*

No.	No. of cycles	σ_{max}^{test} [MPa]	$\sigma_{R0.05}^{10^6}$ [MPa]
1	1,000,000	325	184
	1,000,000	345	
	1,000,000	365	
	1,000,000	385	
	153,644	405	
2	1,000,000	385	193
	1,000,000	405	
	80,476	425	
3	855,122	405	190
4	1,000,000	385	185

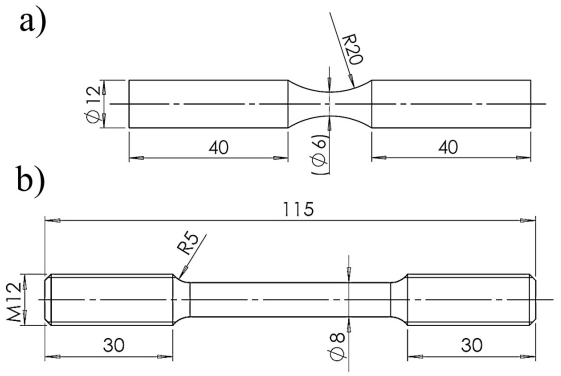

Fig. 5. *Specimen geometry for a) high-strength material and b) low-strength material testing*

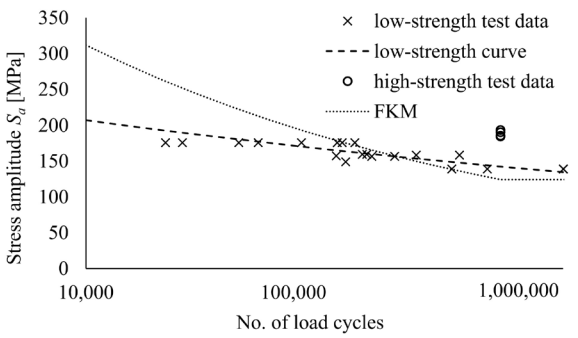

Fig. 6. *Comparison of experimental results and the FKM calculation guideline [16] at $R_{0.05}$ pulsating tensile load for low- and high-strength ISO1083/JS/500-7*

2 FATIGUE LIFE OF ISO1083/JS/500-7 NCI

Table 3 provides a quick view of monotonic tensile strength and tensile fatigue strength at 10^6 cycles of the investigated material. If no tests were conducted at R-1 tension, an estimated value of the fully-reversed fatigue strength obtained by the Goodman approach is shown in brackets for an easier comparison of the different results.

Fig. 7 shows the effect of mean stress on the stress amplitude corresponding to fracture at 10^6 cycles. The modified Goodman approach is used due to its simplicity and slight conservatism for the simulation of the mean stress effect. For the description of the mean test results the mean value of $\sigma_{R-1}^{10^6}$ and the mean value of the yield strength was used to fit the modified Goodman curve.

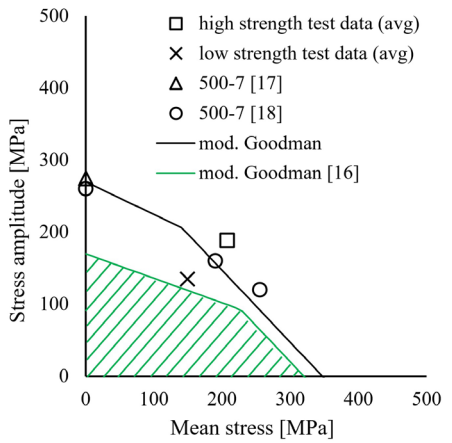

Fig. 7. *Effect of mean stress on the fatigue limit of ISO1083/JS/500-7, experimental results and the modified Goodman curve at 10^6 cycles*

The fatigue data included in the FKM guideline [16] proves to be a good estimate of the low-strength ISO1083/JS/500-7 fatigue properties. Based on FKM [16] data and the modified Goodman approach, a design curve is proposed for the defect-free material by using the values for $\sigma_{R-1}^{10^6}$ and $R_{p0.2}$ from the guideline.

3 FATIGUE LIFE OF MATERIAL WITH SURFACE DISCONTINUITIES

The current study employs four concurrent approaches to simulate the relationship between equivalent surface discontinuity size and the fatigue limit, which is the Kitagawa curve in other terms.

3.1 The Defect Stress Gradient Method

The DSG methodology from Vincent et al. [19] in previous work [Leopold G, Nadot Y. J ASTM Int 7:2010], to represent the effect of a defect in the fatigue criterion by means of a stress gradient term. This general methodology called Defect Stress Gradient (DSG describes the effect of surface discontinuities on the high-cycle fatigue strength under multiaxial loading conditions. The local hot-spot stress is modified with a defect and material-type dependent stress gradient function. In the current analysis, the approach is applied with the Crossland equivalent stress, characterizing the multiaxial fatigue strength of the defect-free material, which limits the application to proportional loading conditions. The Crossland parameters have been identified on the fatigue limits for three different loading types based on the experimental results of Nadot et al. [1] on defect-free NCI, and are $\alpha_{Cr}=1.13$ and $\beta_{Cr}=255$ MPa. The a_{∇} parameter describes the effect of the defect on the multiaxial fatigue strength for spherical surface defects and is $a_{\nabla}=209$ μm.

The equivalent DSG stress σ_{DSG} predicts crack initiation at the value β_{Cr}, and is calculated with the equation:

$$\sigma_{DSG}=\sigma_{Cr}^{\max}-a_{\nabla}\frac{\sigma_{Cr}^{\max}-\sigma_{Cr}^{0}}{\sqrt{area}}\le\beta_{Cr}, \quad (1)$$

where $\sigma_{Cr}^{\max}$ is the maximum of the Crossland equivalent stress at the tip of the defect, σ_{Cr}^{0} is the stress at the same location without the stress concentration effect of the defect. The Crossland equivalent stress is calculated with the following equation for a representative load cycle:

$$\sigma_{Cr}=\sqrt{J_{2\,a}}+\alpha_{Cr}\sigma_{h,\max}. \quad (2)$$

With the simplification, that the ratio $\sigma_{Cr}^{\max}/\sigma_{Cr}^{0}$ is equal to the theoretical elastic stress concentration factor for hemispherical surface defects in an infinite body $K_t^{sph}=2.06$, the allowable hemispherical surface defect size $\sqrt{area}_{all.sph}^{DSG}$ can be expressed according to the following equation:

$$\sqrt{area}_{all.sph}^{DSG}=a_{\nabla}\frac{\sigma_{Cr}^{0}\left(K_t^{sph}-1\right)}{K_t^{sph}\sigma_{Cr}^{0}-\beta_{Cr}}. \quad (3)$$

3.2 The Murakami Approach

The Murakami approach [20] provides a good estimate of the fatigue limit for a large number of different defective materials. It has undergone several smaller developments over the years, which has led to robust applicability. The fatigue limit σ_w can be expressed for a given equivalent defect size $\sqrt{area}$ and load ratio R:

$$\sigma_w=F_{loc}\left(H_V+120\right)\left(\sqrt{area}\right)^{-1/6}\cdot\left[\frac{(1-R)}{2}\right]^{\alpha}, \quad (4)$$

where F_{loc} is the location factor and is 1.43 for a surface defect; α is a material parameter and is given as $0.371+H_V\cdot 10^{-4}$ for NCI material.

The calculation process can be used to express the allowable equivalent defect size $\sqrt{area}_{all.sc}^{Murakami}$ with short crack considerations:

$$\sqrt{area}_{all.sc}^{Murakami}=\left(\frac{F_{loc}\left(H_V+120\right)\left[\frac{(1-R)}{2}\right]^{\alpha}}{\sigma_{1.eff}^{amp}}\right)^{6}. \quad (5)$$

$H_V=200$ hardness was considered for the investigated NCI material as the main input parameter of the Murakami approach.

A differentiation is given for $\sqrt{area}\ge 1000$ μm, where the equivalent crack is considered to be microstructurally long. In this regime, the threshold stress intensity factor (SIF) range for crack propagation is a constant value, estimated as:

$$\Delta K_{th}^{lc}=3.3\cdot 10^{-3}\cdot\left(H_V+120\right)\cdot\sqrt{1000}^{\frac{1}{3}}\cdot\left[\frac{(1-R)}{2}\right]^{\alpha}. \quad (6)$$

This leads to the following equation for the equivalent defect size $\sqrt{area}_{all.lc}^{Murakami}$ with long crack considerations:

$$\sqrt{area}_{all.lc}^{Murakami}=\frac{1}{\pi}\left(\frac{\Delta K_{th}^{lc}}{Y\Delta\sigma_{1.eff}}\right)^{2}. \quad (7)$$

3.3 Fatigue Limit Prediction with Linear Elastic Fracture Mechanics

Considering complete equivalence between surface defects and cracks of equivalent size, linear elastic fracture mechanics (LEFM) can be applied to model the state of the crack propagation threshold, in other

terms the fatigue limit. The NASGRO crack growth model by Forman and Mettu [21] describes the phenomenon of crack closure with a crack-opening function from Newman [22].

The NASGRO model for the NCI material of interest has been calibrated on the experimental results of Björkblad [23]. The threshold stress intensity range in the NASGRO model is calculated as follows:

$$\Delta K_{th} = \Delta K_0 \sqrt{\frac{a}{a + a_0}} \left[\frac{1 - f}{(1 - A_0)(1 - R)} \right], \quad (8)$$

where $a = \sqrt{area}$ is the crack length, $Y = 2/\pi$ is the shape factor at the bottom of a hemispherical surface crack embedded in an infinite body under tension. The material parameters considered in the calculations are summarized in Table 5. The allowable equivalent defect size $\sqrt{area}_{all}^{LEFM}$ according to the LEFM approach is given by:

$$\sqrt{area}_{all}^{LEFM} = \frac{1}{\pi} \left(\frac{\Delta K_{th}}{Y \Delta \sigma_{1.eff}} \right)^2. \quad (9)$$

Table 5. *Material properties for the NASGRO model for ISO1083/JS/500-7, based on experimental data from* [23]

Symbol	Value	Unit
a_0	0.038	mm
α	2.5	-
S_{max} / σ_0	0.3	-
ΔK_0	7.5	$\text{MPa}\sqrt{\text{m}}$
C_{th+}	1	-

3.4 Fatigue Limit Prediction with The Effective Threshold

The equivalence of surface defects and cracks with the same size considered in the LEFM approach is, however, not fully correct. Long fatigue cracks have plastic wake along the crack path, whereas a crack initiated from a defect is a short crack with different parameters to consider in a crack propagation analysis. From a theoretical standpoint, cracks initiated from defects should be modelled with the equivalent size of the defect with the application of the threshold for microstructural crack initiation $\Delta K_{th.eff}$. The effective threshold SIF range is independent of the load ratio. The equivalent allowable defect size can be estimated with the following equation:

$$\sqrt{area}_{all}^{\Delta K_{th.eff}} = \frac{1}{\pi} \left(\frac{\Delta K_{th.eff}}{Y \Delta \sigma_{1.eff}} \right)^2, \quad (10)$$

where $\Delta K_{th.eff} = 3.75\ \text{MPa}\sqrt{\text{m}}$ based on the experimental results of Nadot et al. [24].

3.5 Comparison with Experimental Results

Figs. 8 to 10 show the comparison between the simulated curves with the different methods and the experimental results. The results obtained on specimens with complex artificial defects are displayed with the mean fatigue strength at cycles with a scatter band of three times the standard deviation. Some of the experimental data used for comparison originate from the work of Nadot et al. [1].

The fracture mechanics method based on the effective threshold SIF range ($\Delta K_{th.eff}$) leads to highly conservative results compared to specimens cycled until complete fracture. This approach models the start of microcrack propagation, hence it neglects parts of both the crack initiation and propagation phases. The fracture mechanics method utilizing the threshold SIF range (ΔK_{th}) can lead to non-conservative results in cases of small defects, but overall describes the Kitagawa relationship well at different load ratios. This approach considers complete equivalence between surface defects and fatigue cracks, which can be a non-conservative assumption since cracks initiating from defects do not have the same closure levels as fully formed fatigue cracks of the same size do. The method of Murakami has a good general description of the Kitagawa-curve for ferritic-pearlitic NCI. This approach, however, should be applied carefully, since the utilized $H_V - \Delta K_{th.eff}$ correlation does not necessarily stand for the high-strength ferritic NCI grades. The DSG approach also models the multiaxial fatigue behavior of the defect-free and defective material in the HCF range as well, and therefore more general than the other analysed methods do.

The curves recommended for design have been derived from the curves obtained with the DSG approach with the application of a safety factor estimated from the scatter of the defect-free results for this material grade. The mean stress-dependent safety factor is essentially the distance of the mean experimental and design curves on the Haigh diagram in Fig. 7. Its value is 1.64 for R_{-1}, 1.58 for $R_{0.1}$, and $R_{0.5}$ due to the smaller level of scatter in strength under higher mean stresses.

4 ALLOWABLE DISCONTINUITY SIZE MAPS

The derived formulas for the allowable surface discontinuity size can be used to plot corresponding FE-results for a general complex case. Within the DSG approach the Crossland equivalent stress is employed to describe multiaxial loading effects. For the Murakami and the fracture mechanics-based

approaches, the maximum principal stress range can be used to describe multiaxial stress states, since that corresponds to the crack opening mode in fracture mechanics. It has to be noted, that these criteria are only applicable to proportional loading conditions.

A simple analysis example is employed to demonstrate the allowable discontinuity size FE-results obtainable by the methods introduced in Chapter 3. Fig. 11 shows the analysis setup for a rectangular 3D body under pure bending. The R0 cyclic load was set up with the aim of inducing bending stresses leading to first yield according to the standard proof strength of 320 MPa at the maximum load. E=169 GPa and υ=0.275 were applied to set up the linear elastic material model for the FE-solution. The simulations were conducted with ANSYS Academic Research 17.2 software.

Fig. 12 shows the allowable discontinuity size maps obtained by the different approaches. The

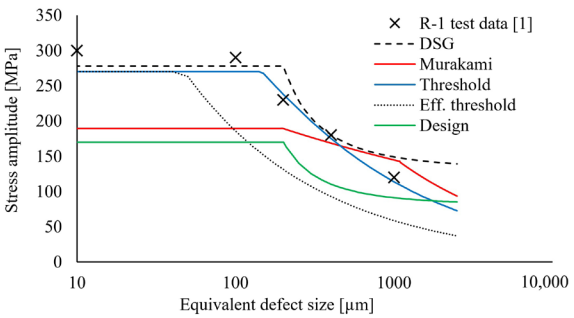

Fig. 8. *Kitagawa curves for R_{-1} tension-compression for NCI with artificial surface defects, with additional experimental results from* [1]

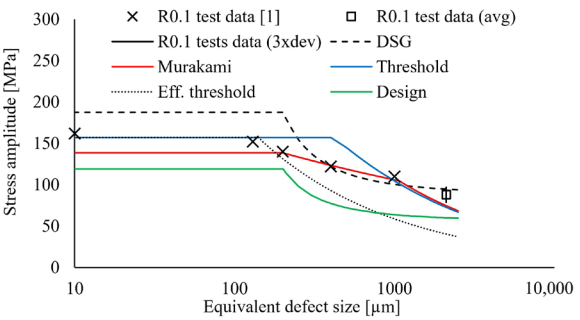

Fig. 9. *Kitagawa curves for $R_{0.1}$ tension for NCI with artificial surface defects, with additional experimental results from* [1]

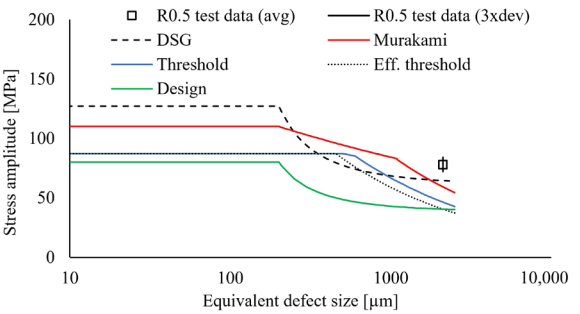

Fig. 10. *Kitagawa curves for NCI under $R_{0.5}$ tension loading with artificial surface defects*

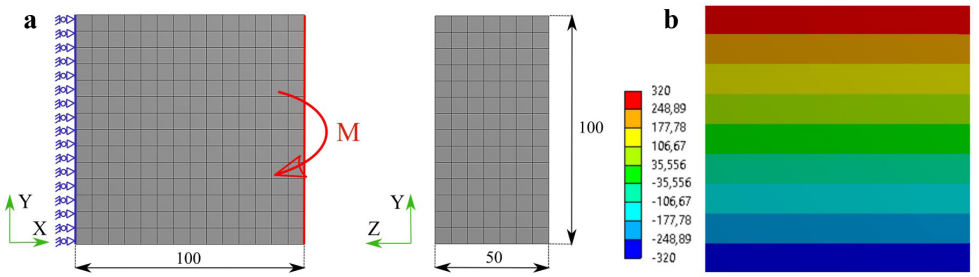

Fig. 11. *a) FEA model setup and b) the normal stress [MPa] result field at the maximal load*

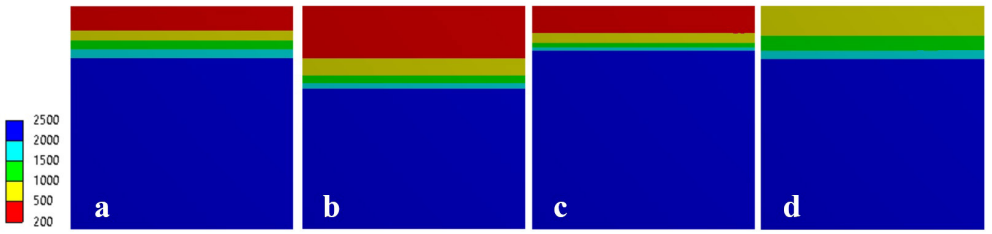

Fig. 12. *Allowable discontinuity size FE-result fields with a) Murakami's, b) effective threshold, c) DSG and d) LEFM approaches*

differences of the compared approaches follow the trend discussed in Chapter 3.5. Fig. 13 displays the design values of the allowable surface discontinuity size derived from the results obtained with the DSG approach with the application of the mean stress-dependent safety factor. Illustrations of the corresponding discontinuity sizes are linked with the different colour bands to provide some level of physical connection. From the illustration of the proposed methodology, it can be concluded that even large surface defects can be tolerable from the standpoint of safe in-service life, if their position on the component is carefully monitored. In the current case displayed on Fig. 13, 1 mm to 1.5 mm surface defects can be allowed on more than two thirds of the component surface, which is marked by blue on the defect size map. (The legend indicates 1.5 mm to 2 mm for this colour band, but the distribution inside one band is unknown. For this reason, the allowed defect size range is shifted to a lower class.) The area-ratio of the different colour bands is governed by the nature of the Kitagawa diagram, which shows a decreasing sensitivity (especially the DSG approach) to the increase of the defect size in the investigated range. The critical area, where no discontinuities are allowed, must be generally quite narrow, otherwise the component would not even comply with the traditional fatigue assessment.

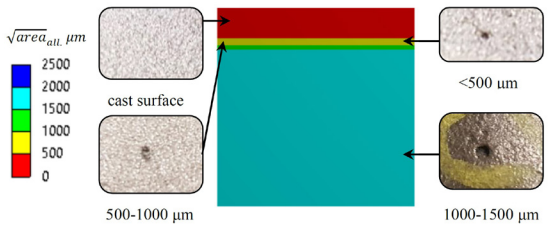

Fig. 13. *Allowable discontinuity size FE-result field for design with the DSG approach*

5 CONCLUSIONS

Fatigue tests have been conducted to analyse the scatter of fatigue properties for the ISO1083/JS/500-7 NCI material grade. A 40 % difference in the fatigue strength ($\sigma_{R0.05}^{10^6}$) is possible between polished samples machined from 500-7 NCI components. The step-by-step [2] approach has proven to give good results for the analysed material; the loading history below the fatigue limit had a negligible effect on the fatigue strength at load cycles. Different methods applicable to the assessment of surface discontinuities have been compared in the current paper.

Allowable surface defect size maps have been plotted for a simple analysis example: for the comparison of the methods in their planned field of application. Surface discontinuities of 1000 µm can reduce the fatigue strength of NCI by a factor of 2.5. (hemispherical defects in cylindrical test specimens under R_{-1} tension-compression [1]).

The fracture mechanics method based on the effective threshold SIF range ($\Delta K_{th.eff}$) leads to highly conservative results compared to specimens cycled till complete fracture.

The fracture mechanics method utilizing the threshold SIF range (ΔK_{th}) can lead to non-conservative results in case of small defects, but overall describes the Kitagawa relationship well at different load ratios.

The method of Murakami has a good general description of the Kitagawa-curve for ferritic-pearlitic NCI. This approach however should be applied carefully, since the utilized H_V–ΔK_{th} correlation does not necessarily stand for the high-strength ferritic NCI grades.

The DSG approach also models the multiaxial fatigue behaviour of the defect free and defective material in the HCF range and is, therefore, more general than the other analysed methods.

The fatigue properties recommended by the FKM Guideline [16] are in good agreement with the tested low-strength ISO1083/JS/500-7 material; they truly represent the lower end mechanical properties for this grade.

6 ACKNOWLEDGEMENTS

The recent study was realized within the Knorr-Bremse Scholarship Program supported by the Knorr-Bremse Rail Systems Budapest.

7 NOMENCLATURES

a_∇	material parameter in the DSG criterion, [µm]
a_0	material constant depending on the microstructure, [mm]
A_0	component of the crack-opening function by Newman, [-]
$\sqrt{area}$	equivalent defect size from Murakami, [MPa]
C_{th+}	fitting parameter describing the R-dependence of ΔK_{th}, [-]
E	modulus of elasticity, [GPa]
f	crack-opening function by Newman, [-]
F_{loc}	location factor, [MPa]
H_V	Vickers hardness, [MPa]

$\sqrt{J_{2\,a}}$	amplitude of the square root of the second invariant of the deviatoric stress tensor in a load cycle, [MPa]
R	fatigue load ratio, [-]
$R_{p0.2}$	monotonic proof strength at 0.2 % elongation, [MPa]
R_m	ultimate tensile strength, [MPa]
$S_{\max}/\sigma_0$	ratio of the maximum applied stress to the flow stress in the NASGRO model, [-]
α	plane stress/plain strain constraint, [-]
α_{Cr}	material parameter in the Crossland criterion, [-]
β_{Cr}	material parameter in the Crossland criterion, [MPa]
ΔK_0	the value of ΔK_{th} at R_0, [MPa√m]
ΔK_{th}	crack propagation threshold stress intensity factor range, [MPa√m]
$\Delta K_{th.eff}$	effective value of the threshold stress intensity factor, [MPa√m]
σ_{max}^{test}	applied cyclic stress max., [MPa]
$\sigma_a^{10^6}$	fatigue strength in stress amplitude at 10^6 cycles, [MPa]
$\sigma_{RX}^{10^6}$	fatigue strength in stress amplitude at 10^6 cycles and load ratio "X", [MPa]
σ_{Cr}	Crossland equivalent stress, [MPa]
$\sigma_{h,\max}$	max. of the hydrostatic stress in a load cycle, [MPa]
σ_w	fatigue limit for a given load-ratio, [MPa]
$\sigma_{1.eff}^{amp}$	the effective maximum principal stress amplitude, [MPa]
$\Delta\sigma_{I.eff}$	the effective maximum principal stress range, [MPa]
υ	Poisson's ratio, [-]

8 REFERENCES

[1] Nadot, Y., Mendez, J., Ranganathan, N., (2004). Influence of casting defects on the fatigue limit of nodular cast iron. *International Journal of Fatigue*, vol. 26, no. 3, p. 311-319, **DOI:10.1016/S0142-1123(03)00141-5**.

[2] Bellows, R.S., Muju, S., and Nicholas, T. (1999). Validation of the step test method for generating haigh diagrams for Ti – 6Al – 4V. *International Journal of Fatigue*, vol. 21, no. 7, p. 687-697, **DOI:10.1016/S0142-1123(99)00032-8**.

[3] Cheng, Z., Liao, R., Lu, W., Wang, D. (2017). Fatigue notch factors prediction of rough specimen by the theory of critical distance. *International Journal of Fatigue*, vol. 104, p. 195-205, **DOI:10.1016/j.ijfatigue.2017.07.004**.

[4] Rotella, A., Nadot, Y., Augustin, R., Piellard, M., L'Heritier, S. (2017). Defect size map for cast A357-T6 component under multiaxial fatigue loading using the defect stress gradient (DSG) criterion. *Engineering Fracture Mechanics*, vol. 174, p. 227-242, **DOI:10.1016/j.engfracmech.2016.12.008**.

[5] Vincent, M., Nadot, Y., Nadot-Martin, C., Dragon, A. (2016). Interaction between a surface defect and grain size under high cycle fatigue loading: Experimental approach for Armco iron. *International Journal of Fatigue*, vol. 87, p. 81-90, **DOI:10.1016/j.ijfatigue.2016.01.013**.

[6] Schönbauer, B.., Yanase, K., Endo, M. (2017). Influences of small defects on torsional fatigue limit of 17-4PH stainless steel. *International Journal of Fatigue*, vol. 100, part 2, p. 540-548, **DOI:10.1016/j.ijfatigue.2016.12.021**.

[7] Mukherjee, K., Fæster, S., Hansen, N., Dahl, A.B., Gundlach, C., Frandsen, J.O., Sturlason, A. (2017). Graphite nodules in fatigue-tested cast iron characterized in 2D and 3D. *Materials Characterization*, vol. 129, p. 169-178, **DOI:10.1016/j.matchar.2017.04.024**.

[8] Ostash, O.P., Chepil, R.V., Vira, V.V. (2017). On the assessment of fatigue life of notched structural components. *International Journal of Fatigue*, vol. 105, p. 305-311, **DOI:10.1016/j.ijfatigue.2017.09.007**.

[9] Gates, N., Fatemi, A. (2016). Notch deformation and stress gradient effects in multiaxial fatigue. *Theoretical and Applied Fracture Mechanics*, vol. 84, p. 3-25, **DOI:10.1016/j.tafmec.2016.02.005**.

[10] Liu, J., Zhang, R., Wei, Y., Lang, Sh. (2017). A new method for estimating fatigue life of notched specimen. *Theoretical and Applied Fracture Mechanics*, **DOI:10.1016/j.tafmec.2017.07.017**.

[11] ISO 1083:2004(E). *Spheroidal Graphite Cast Irons – Classification*. International Organization for Standardization, Geneva, p. 31.

[12] Murakami, Y. (2002). *Metal Fatigue: Effects of Small Defects and Nonmetallic Inclusions*, Elsevier Science, Oxford.

[13] ISO 945-1:2017. *Microstructure of Cast Irons – Part 1: Graphite Classification by Visual Analysis*, International Organization for Standardization, Geneva.

[14] DIN 50125:2016-12. T*esting of metallic materials - Tensile test pieces*, DIN, Berlin.

[15] ISO 6892-1:2016. *Metallic Materials - Tensile Testing - Part 1: Method of Test at Room Temperature*, International Organization for Standardization, Geneva.

[16] FKM (2012). *Analytical Strength Assesment of Components*, VDMA Verlag, Frankfurt am Main.

[17] Yamabe, J., Kobayashi, M. (2006). Influence of casting surfaces on fatigue strength of ductile cast iron. *Fatigue & Fracture of Engineering Materials & Structures*, vol. 29, no. 6, p. 403-415, **DOI:10.1111/j.1460-2695.2006.01017.x**.

[18] Rabb, B.R. (2004). Influence of Occasional Underloads on Fatigue. *European Congress on Computational Methods in Applied Science and Engineering*, Jyväskylä, p. 229-250.

[19] Vincent, M., Nadot-Martin, C., Nadot, Y., Dragon, A. (2014). Fatigue from defect under multiaxial loading: defect stress gradient (DSG) approach using ellipsoidal equivalent inclusion method. *International Journal of Fatigue*, vol. 59, p. 176-187, **DOI:10.1016/j.ijfatigue.2013.08.027**.

[20] Murakami, Y. (2002). *Mechanism of Fatigue in the Absence of Defects and Inclusions. Metal Fatigue: Effects of Small Defects and Nonmetallic Inclusions*. Elsevier Science Oxford, **DOI:10.1016/B978-008044064-4/50001-3**.

[21] Forman, G.R., Mettu, S.R. (1990). Behavior of surface and corner cracks subjected to tensile and bending loads in Ti-6A1-4V Alloy, *NASA Technical Memorandum*, NASA, Houston.

[22] Newman, J.C. Jr. (1984). A crack opening stress equation for fatigue crack growth. *International Journal of Fracture*, vol. 24, no. 4, p. R131-R135, **DOI:10.1007/BF00020751**.

[23] Björkblad, A. (2005). Conventional vs. closure free crack growth in nodular iron. Samuelsson, J., Marquis, G. (eds.). *Competent Design by Castings Conference: Improvements in a Nordic Project*, p. 273-286.

[24] Nadot, Y., Mendez, J., Ranganathan, N., Beranger, A.S. (1999). Fatigue life assessment of nodular cast iron containing casting defects. *Fatigue & Fracture of Engineering Materials & Structures*, vol. 22, no. 4, p. 289-300, **DOI:10.1046/j.1460-2695.1999.00162.x**.